Nano Research 2015, 8(3): 851–859
DOI 10.1007/s12274-014-0567-z
Research Article

ISSN 1998-0124
CN 11-5974/O4

Laser induced oxidation and optical properties of stoichiometric and non-stoichiometric Bi_2Te_3 nanoplates

Rui He[1] (✉), Sukrit Sucharitakul[2], Zhipeng Ye[1], Courtney Keiser[1], Tim E. Kidd[1], and Xuan P. A. Gao[2]

[1] *Department of Physics, University of Northern Iowa, Cedar Falls, Iowa 50614, USA*
[2] *Department of Physics, Case Western Reserve University, Cleveland, Ohio 44106, USA*

Received: 1 July 2014
Revised: 11 August 2014
Accepted: 18 August 2014

KEYWORDS
bismuth telluride,
nanoplate,
Raman spectroscopy,
oxidation,
stoichiometry

ABSTRACT

Bi–Te nanoplates (NPs) grown by a low pressure vapor transport method have been studied by Raman spectroscopy, atomic force microscopy (AFM), energy-dispersive X-ray spectroscopy (EDS), and Auger electron spectroscopy (AES). We find that the surface of relatively thick (more than tens of nanometers) Bi_2Te_3 NPs is oxidized in the air and forms a bump under heating with moderate laser power, as revealed by the emergence of Raman lines characteristic of Bi_2O_3 and TeO_2 and characterization by AFM and EDS. Further increase of laser power burns holes on the surface of the NPs. Thin (thicknesses less than 20 nm) NPs with stoichiometry different from Bi_2Te_3 were also studied. Raman lines from non-stoichiometric NPs are different from those of stoichiometric ones and display characteristic changes with the increase of Bi concentration. Thin NPs with the same thickness but different stoichiometries show different color contrast compared to the substrate in the optical image. This indicates that the optical absorption coefficient in thin Bi–Te NPs strongly depends on their stoichiometry.

1 Introduction

Bi–Te thin films and nanostructures are important materials for thermoelectric (TE) and electronic device applications. Stoichiometric Bi_2Te_3 (40% Bi and 60% Te) is of particular interest because it is a representative topological insulator (TI) with a single Dirac cone on the surface [1–4] and a typical TE material with low thermal conductivity [5–7]. Bi_2Te_3 crystallizes in a layered structure with quintuple layers ordered in a Te-Bi–Te–Bi–Te sequence. Bi–Te films with other molar content percentages such as BiTe (50% Bi and 50% Te) and Bi_4Te_3 (57% Bi and 43% Te) have different crystalline structures [8, 9] and different vibrational properties [10] compared to the stoichiometric Bi_2Te_3 counterpart. It has been shown that a deviation (even as small as 0.1%) of Bi:Te atomic ratio from stoichiometry has a large impact on the electronic and TE properties of Bi_2Te_3 material [11, 12]. Moreover, fine tuning of the doping and stoichiometry of telluride and related chalcogenides turns out to be central to the control of topological surface transport in the research of three-dimensional TIs [13–16]. Understanding the fundamental physical properties of Bi–Te thin films

Address correspondence to rui.he@uni.edu

and nanostructures with different thicknesses and stoichiometries is thus crucial to various applications of these materials.

In this paper we present our studies of Bi–Te nanoplates (NPs) grown by a low pressure vapor transport method. We use Raman spectroscopy, atomic force microscopy (AFM), energy-dispersive X-ray spectroscopy (EDS), and Auger electron spectroscopy (AES) to characterize the composition, morphology and to study the optical and vibrational properties of Bi–Te thin layers. Raman scattering from relatively thick (at least tens of nanometers thick) Bi–Te NPs shows four Raman peaks (at low laser power) that overlap those from bulk Bi_2Te_3, which indicates that these relatively thick layers form Bi_2Te_3 bulk phase. At intermediate laser power the surface of these Bi_2Te_3 layers forms a bump, and an increase of oxygen concentration is observed at the laser spot in the EDS map. Characteristic Raman lines from Bi_2O_3 and TeO_2 appear in the Raman spectrum. Therefore, Bi_2Te_3 surface is oxidized under laser heating with intermediate power. As the laser power is further increased, holes are burned on the sample surface, and the depth of the holes increases at higher laser power.

In Bi–Te NPs thinner than 20 nm, Raman signals are different from those of Bi_2Te_3 phase. A new mode centered at ~93 cm^{-1} appears in the Raman spectra, and the position of the highest frequency Raman mode varies significantly in NPs with even the same thickness. Optical images show that NPs with the same thickness have very different color contrast with the substrate. The difference in the Raman peaks and color contrast in NPs with the same thickness is attributed to the variation in stoichiometry (confirmed by AES) and concomitant change in the optical absorption coefficient α. An α-versus-stoichiometry plot suggests that α may experience a dramatic change when the Bi atomic content is about 45%.

2 Experimental procedures

In this work Bi_2Te_3 NPs were grown by low pressure vapor transport with similar setup as in our previous work [17] and in the work done by Kong et al. [18]. Bi_2Te_3 flakes (99.999%, Alfa Aesar) were ground thoroughly. An amount of 80 mg of the resulting powder was transferred to a quartz crucible placed at the center of a single-zone tube furnace (Lindberg Blue M) as the vapor precursor for the growth. A 1 cm × 5 cm Si wafer with 300 nm oxide layer was rinsed with acetone, ethanol and deionized (DI) water for 10 s each. Then the substrate wafer was dried with compressed air followed by ozone cleaning for 10 min at room temperature. The cleaned wafer was placed 11.5 cm away from the center of the furnace downstream. The system was pumped down to a base pressure of 20 mTorr and flushed with 100 standard cubic centimeters per minute (sccm) of Ar (10% H_2) gas for 1 min. The pressure was later adjusted to 500 mTorr, and the Ar flow rate was reduced to 40 sccm. To eliminate any residue humidity in the system, the furnace was heated to 100 ˚C for 30 min prior to the growth. The precursor (Bi_2Te_3 powder) temperature was then raised to 540 ˚C (leaving growth temperature on the substrate to be approximately 420 ˚C) and kept constant for 5 min. Once the growth process finished, the system was cooled down to the room temperature.

A photolithography process was conducted on another cleaned SiO_2/Si wafer to make patterned metal features as references for samples' coordinates or bases for suspending samples. Using LOR3A and S1805 (Microchem™) copolymer/polymer bilayer standard spin coating and baking recipe, photolithography patterns were made after UV light exposure over the photo mask for 2.50 s prior to development in CD-26 (Microposit MF) developer for 70 s. The wafer was then rinsed in DI water for 30 s and dried with compressed air. Afterwards, 5-nm-thick Cr and 70-nm-thick Ni were evaporated over the wafer before the removal of the remaining photoresist with PG remover solution.

Bi_2Te_3 NPs were transferred by contact printing method. The prepared SiO_2/Si wafer with Ni metal patterns was gently pressed against the growth wafer to transfer Bi–Te NPs and to create suspended NPs. The wafer with transferred NPs was later rinsed with ethanol and DI water then dried with compressed air for final cleaning prior to further characterization.

Raman spectra were recorded at room temperature using a Horiba HR Raman Microscope system equipped with thermoelectric cooled charge-coupled

device (CCD) multichannel detection. A laser with 532 nm excitation was used. The laser light was focused by a 100× objective lens (spot diameter of ~1 μm). Instrument resolution was ~0.5 cm^{-1} using the 1,800 groove/mm grating. Laser power up to 10 mW was used to study the laser induced oxidation and burning of the Bi–Te NPs. EDS measurements were performed using a Bruker Quantax system connected to a TESCAN Vega II scanning electron microscope. AFM scans were conducted using an Agilent AFM 5500. AES measurements were performed by using a PHI 680 system.

3 Results and discussion

3.1 Laser induced oxidation and damage in stoichiometric Bi_2Te_3 NPs

Figure 1(a) shows Raman spectra from a 114-nm-thick Bi–Te NP excited with different laser power. When the laser power is low (≤0.1 mW), the spectra show a weak mode centered at ~37 cm^{-1} and three well-defined Raman lines at 62, 102, and 134 cm^{-1}. The frequencies of these four peaks (highlighted by solid vertical lines in Fig. 1(a)) overlap those of Raman-active modes (E_g^1, A_{1g}^1, E_g^2, A_{1g}^2) from bulk Bi_2Te_3 [19, 20]. Considering that these four peaks are the only ones seen in the Raman spectra, we can safely conclude that this Bi–Te NP has Bi_2Te_3 stoichiometry. The surface of this Bi_2Te_3 NP does not show any visible change after excitation with low laser power (≤0.1 mW).

In Fig. 1(a) we can see that when the laser power increases to an intermediate level of 1 mW, the Raman spectrum from the same NP changes dramatically. Raman intensities from all modes increase significantly compared to those excited with low laser power. The E_g^1, A_{1g}^1, and E_g^2 modes all shift to lower frequency

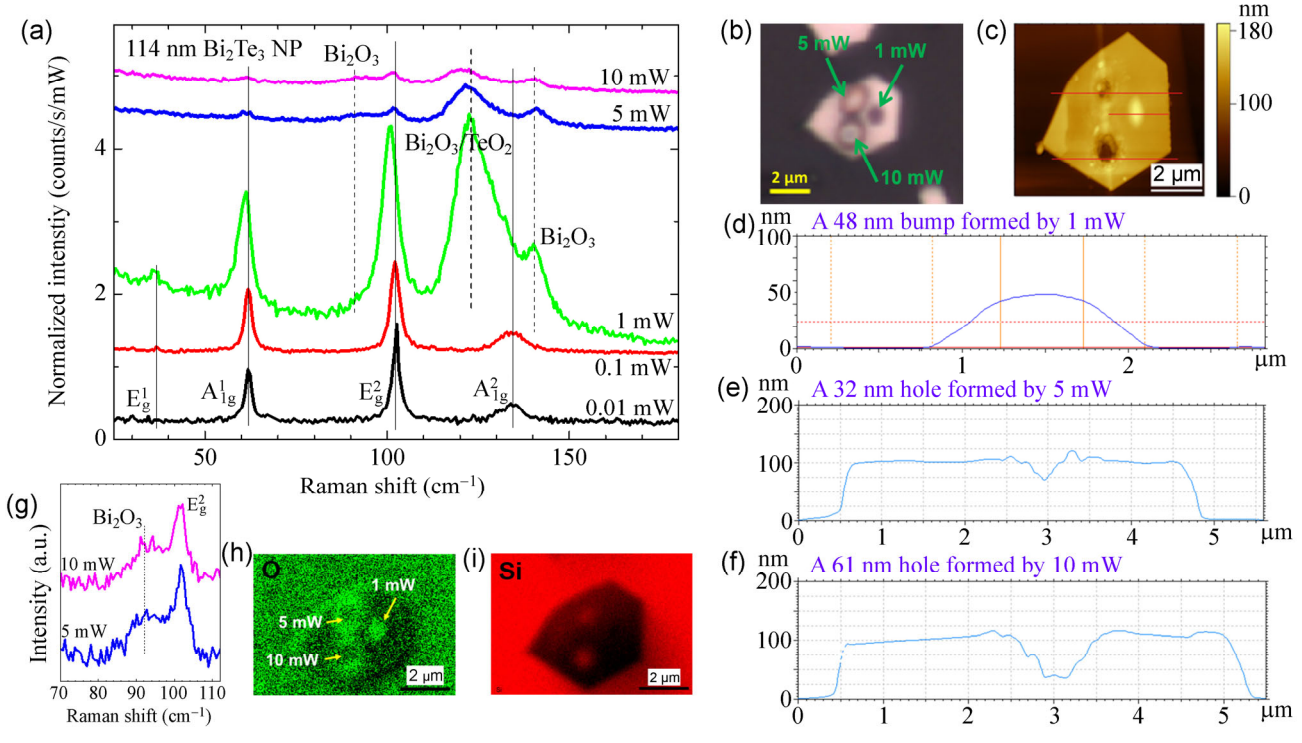

Figure 1 (a) Raman spectra excited by different laser power from a 114-nm-thick Bi_2Te_3 NP on SiO_2. The integration time for each spectrum (from bottom to top) is 420, 60, 10, 5, and 3 s. The solid vertical lines highlight the positions of the four Raman-active modes in crystalline Bi_2Te_3. The dashed vertical lines highlight the positions of the Raman lines from Bi_2O_3 and TeO_2. (b) Optical image of this 114-nm-thick Bi_2Te_3 NP. The bump and holes created on the sample surface with different laser power are labeled. (c) AFM image of this NP. (d), (e), and (f) Step-height analyses of the bump and holes formed on the sample surface along the three scanning lines shown in panel (c). (g) Zoomed-in spectra that are excited by the 5 and 10 mW laser power. The Raman line at ~91 cm^{-1} (due to Bi_2O_3) is highlighted by a dashed vertical line. (h) and (i) EDS maps of oxygen and Si concentrations.

possibly due to expanded crystal lattice and reduced interlayer/interatomic interactions at elevated temperature. The most prominent change in the Raman spectrum is the emergence of two strong and broad bands centered around 123 and 140 cm^{-1} and a weak shoulder centered at about 91 cm^{-1} on the low energy side of the E_g^2 mode. The dashed vertical lines in Fig. 1(a) highlight the positions of these three new bands.

We can see in the optical image shown in Fig. 1(b) that a dark spot is formed on the sample surface after illumination by the intermediate laser power of 1 mW. AFM image and step height analysis (see Figs. 1(c) and 1(d)) show that this area forms a bump with a height of ~50 nm, close to half of the thickness of the original Bi_2Te_3 NP. EDS mapping of the oxygen concentration shown in Fig. 1(h) suggests that the concentration of oxygen at this spot illuminated by 1 mW laser is higher compared to other areas that are not exposed to the laser. After comparing the frequencies of the three new Raman bands with those from Bi_2O_3 and TeO_2 [21–23], we assign the new peaks at ~91 and ~140 cm^{-1} to the vibrational modes from Bi_2O_3. The broad band centered at ~123 cm^{-1} could be from both Bi_2O_3 and TeO_2. The A_{1g}^2 mode at 134 cm^{-1} that appears in low power Raman spectra is obscured by the broad Bi_2O_3 and TeO_2 features at the intermediate (1 mW) laser power.

As the laser power further increases (see the spectra excited by 5 and 10 mW in Fig. 1(a)), the intensities from all Raman modes decrease. However, the relative intensity between the 91 cm^{-1} mode (from Bi_2O_3) and the E_g^2 mode of Bi_2Te_3 becomes stronger (see Fig. 1(g)) compared to that in the spectrum excited by 1 mW laser power (see Fig. 1(a)). In the optical image shown in Fig. 1(b) we can see laser induced damage on the sample surface (two holes burned by 5 and 10 mW laser irradiation). AFM analysis shown in Figs. 1(c), 1(e), and 1(f) indicates that an approximately 30-nm-deep hole was burned on the sample surface with 5 mW laser irradiation, and an even deeper hole of at least 60-nm depth was burned on the sample surface with 10 mW laser illumination. On the edges of the holes, the surfaces form ring-like bumps as revealed in the AFM step-height analysis (see Figs. 1(e) and 1(f)) and EDS mapping of oxygen concentration displayed in Fig. 1(h). It is seen that the oxygen concentration is higher at the edges of the holes compared to other areas that are not illuminated by the laser light. At the two burned holes, the electron beam penetrates deeper into the Si substrate which leads to higher readings of Si concentration at the two sites in EDS mapping (see Fig. 1(i)).

These power-dependent Raman studies and characterizations by AFM and EDS show that Bi_2Te_3 crystalline structure is stable under low laser power irradiation (much lower than 1 mW) [11]. As the laser power increases to an intermediate level (~1 mW), the sample surface becomes oxidized and forms a bump protruding on the surface with an expanded lattice. Further increase of the laser power not only causes oxidation but also burns holes on the sample surface. The higher the laser power, the deeper the holes are. It is worthwhile noting that the oxidation of Bi_2Te_3 NP surfaces is mainly associated with the laser power used to perform the Raman measurement. Under the low laser power irradiation (e.g., 0.1 mW), no damage on the Bi_2Te_3 NP surface was observed for a relatively long irradiation time (120 s, see Fig. S1 in the Electronic Supplementary Material (ESM)). However, if the laser power increases to an intermediate level of ~1 mW, the sample surface became oxidized within a short amount of illumination time (1.5 s, Fig. S2 in the ESM). Longer irradiation time at this laser power leads to stronger Raman signals from Bi_2O_3 and TeO_2 (see Fig. S2 in the ESM). This suggests that within the time scale that is typically used to perform Raman characterization of Bi_2Te_3 nanostructures, laser power is the main parameter that one needs to control in order to avoid laser-induced oxidation and damage on the sample surface.

3.2 Lattice vibrations in Bi–Te thin NPs

Figure 2(a) shows an optical image of a 15-nm-thick Bi–Te NP that is partially supported by Ni pattern and partially suspended. Figures 2(b) and 2(c) show the Raman spectra excited by different laser power on the supported and suspended areas on this NP. Four Raman peaks (P1–P4) are seen in each spectrum and highlighted by vertical dashed lines. The origin of these Raman peaks will be discussed in more detail later in the paper. In Figs. 2(b) and 2(c) we can see that

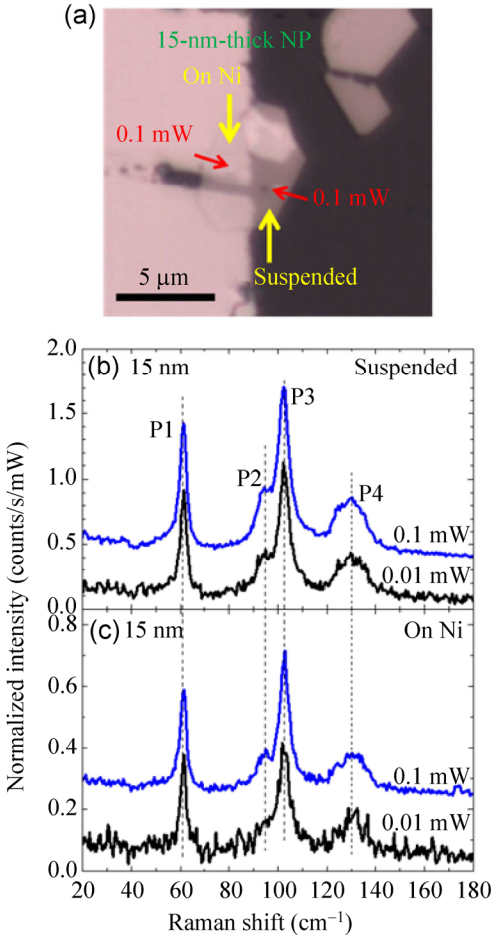

Figure 2 (a) Optical image of a 15-nm-thick Bi–Te NP that is suspended on Ni. The Ni layer has a thickness of 70 nm and is evaporated on SiO_2 substrate. A small dark spot is seen on the suspended part under 0.1 mW laser irradiation. (b) Raman spectra excited by different laser power from suspended area on the Bi–Te NP shown in panel (a). The acquisition time is 420 and 120 s for 0.01 and 0.1 mW laser power, respectively. The vertical dashed lines highlight the positions of the four Raman peaks. (c) Same as in (b) on the area supported by Ni. The acquisition time is 540 and 120 s for 0.01 and 0.1 mW laser excitation, respectively.

the spectra from supported and suspended areas are similar without prominent changes in peak positions and linewidths. The similarity suggests that the interaction between the Bi–Te NP and the substrate is relatively weak. Both areas do not show any damage after illuminated by 0.01 mW laser power. However, 0.1 mW laser irradiation can damage the suspended area (a black spot formed on the suspended area after laser irradiation as shown in Fig. 2(a)) but not the portion that is supported by the Ni pattern. This difference could be attributed to the increased efficiency of heat dissipation for the portion of the NP that is supported by the substrate. Although the optical image of the sample shows a damaged spot in the suspended area after 0.1 mW laser irradiation, the Raman spectrum does not show strong features of Bi_2O_3 and TeO_2. This absence of strong Bi_2O_3 and TeO_2 Raman lines has two possible causes. The first is related to the thickness of the sample. In thin (< 20 nm) NPs, the height of any bumps formed on the sample surface due to laser illumination is much smaller than that found on thick stoichiometric Bi_2Te_3 NP surfaces (bumps of several tens of nm tall). Therefore, Raman signals from the bumps (oxidized areas) on the thin NPs are expected to be very weak. The second reason is related to the stoichiometry of the NP. This thin NP has a Bi-rich stoichiometry that differs from Bi_2Te_3 (see the discussion below). The deviation of Bi–Te atomic ratio could lead to different thermal transport properties and different oxidation rate compared to those occur in stoichiometric samples. Further investigations are needed to understand the impact of stoichiometry on the oxidation processes in thin Bi–Te NPs.

Figures 3(a) and 3(b) show Raman spectra from thin Bi–Te NPs (thicknesses less than 20 nm) that are supported on SiO_2 substrate and are suspended, respectively. In order to avoid laser heating induced damage, we used the lowest laser power of 0.01 mW to take all the spectra. The positions of peaks P1, P3, and P4 are close to those of the A_{1g}^1, E_g^2, and A_{1g}^2 Raman lines seen in crystalline Bi_2Te_3. The mode P2 is centered at about 93 cm^{-1}. This mode cannot be assigned to the characteristic Bi_2O_3 vibration because laser induced oxidation is negligible at this power level [11, 24]. This P2 mode cannot be attributed to the infrared (IR)-active mode A_{1u}^1 either [19] for the following two reasons. First, the relative intensity between this P2 mode and other Raman-active modes (P1, P3, and P4) does not increase monotonically with the reduction of NP thickness. The presence of IR-active mode A_{1u}^1 in ultrathin Bi_2Te_3 NPs has been observed and ascribed to a breakdown of inversion symmetry in TI nanostructures [20]. Hence, the relative intensity between the IR-active and Raman-active modes increases in thinner layers [25]. However, this is not what we observed in Bi–Te thin NPs with various thicknesses (Figs. 3(a) and 3(b)). Second, all

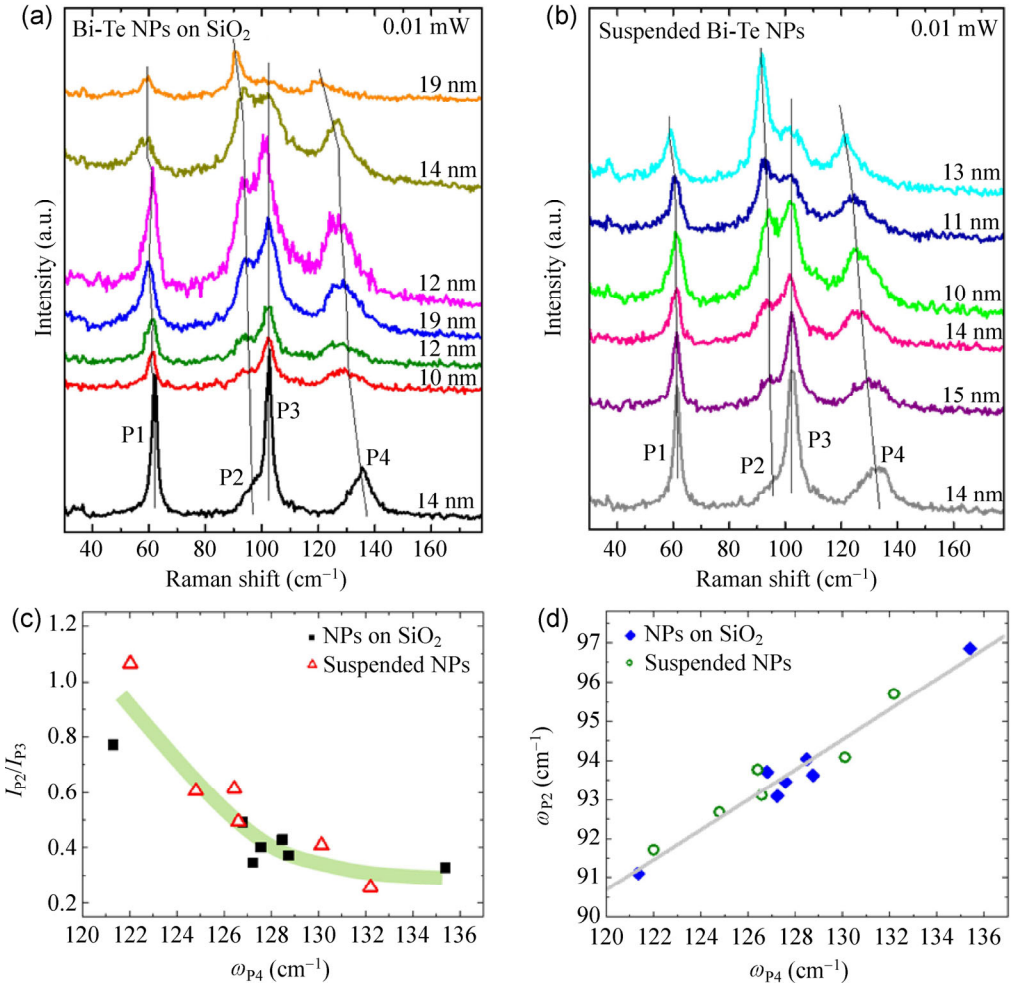

Figure 3 (a) Raman spectra from thin Bi–Te NPs (with different thicknesses) on SiO_2 substrates. The laser power is 0.01 mW for all the spectra. The solid lines highlight the positions of the four Raman peaks. (b) Same as in (a) for suspended NPs. (c) Intensity ratio of P2 and P3 as a function of the frequency of P4 from both supported and suspended Bi–Te NPs. (d) Frequency of P2 as a function of that of P4 for both supported and suspended NPs. The solid lines in panels (c) and (d) are guides to the eye.

the NPs we studied in this work were transferred to a second SiO_2 substrate with Ni patterns after growth. IR-active modes are usually only observed in as-grown NPs. The transferred ones have relatively weak interaction with the substrates and thus do not show inversion symmetry breaking (IR-active modes) [20]. Based on these considerations, the P2 mode at around 93 cm^{-1} that we observed in thin NPs (all transferred) is unlikely to be the A_{1u}^1 IR-active mode from Bi_2Te_3 NPs. Comparing the Raman spectra from our thin NPs with those from non-stoichiometric Bi_2Te_3 films [10], we assign the P2 mode to one of the Raman modes from Bi-rich (over 40%) Bi–Te structures. Because the crystalline structures and space groups of non-stoichiometric Bi–Te layers are not necessarily the same as those of Bi_2Te_3 [8, 10], we do not use the same symmetry symbols (E_g^1, A_{1g}^1, E_g^2, A_{1g}^2) as we use to denote Raman modes observed in thicker Bi_2Te_3 NPs to label the four vibrational modes (P1–P4) seen in these off stoichiometric Bi–Te thin NPs.

The atomic ratio of Bi–Te has a large impact on the Raman spectra. As the Bi molar content percentage increases beyond 40%, Raman peaks shift and the relative intensity between P2 and P3 increases monotonically [10]. Therefore, we plot the spectra in Figs. 3(a) and 3(b) in the order of increasing intensity ratio between P2 and P3. From the relative intensities between these two modes, we estimate that the atomic concentration of Bi in our thin NPs is between 40%–57% (Bi-rich in comparison to Bi_2Te_3 stoichiometry).

Figure 3(c) shows the ratio of integrated intensities of P2 and P3 (I_{P2}/I_{P3}) as a function of the frequency of P4 (ω_{P4}). The solid points are from Bi–Te NPs on SiO_2, and the empty ones are from suspended NPs. It is seen that in the spectra from both supported and suspended NPs, I_{P2}/I_{P3} decreases monotonically with the increase of ω_{P4}. Figure 3(d) shows that the Raman frequency of mode 2 (ω_{P2}) increases linearly with the increase of ω_{P4}. Because I_{P2}/I_{P3} increases monotonically with the atomic concentration of Bi [10], these results shown in Figs. 3(c) and 3(d) suggest that ω_{P2} and ω_{P4} may also be used to characterize the Bi concentration in Bi–Te crystals.

3.3 Optical absorption of Bi–Te thin NPs

Figures 4(a) and 4(b) show the optical images of two Bi–Te NPs with the same thickness of 19 nm. The Raman spectra from these two NPs are displayed in Fig. 3(a) (the topmost one is for the NP shown in Fig. 4(a) and the one in the middle is from the NP shown in Fig. 4(b)). The color contrast with the SiO_2 substrate background is very different for the two NPs. The one shown in Fig. 4(a) looks much brighter compared to the substrate. The difference in color contrast indicates that the optical absorption coefficient at this incident laser wavelength (532 nm) differs significantly in the two NPs.

We estimate the optical absorption coefficients by measuring the Raman signals of Si before and after the laser light penetrates the NPs. Raman spectra from the bare substrate and after the laser light penetrates the two NPs are shown in Fig. 4(c). It is seen that the laser light is strongly absorbed by the two NPs, and the absorption by the one shown in Fig. 4(a) is even stronger. The optical absorption coefficient α at λ = 532 nm of the NPs can be estimated

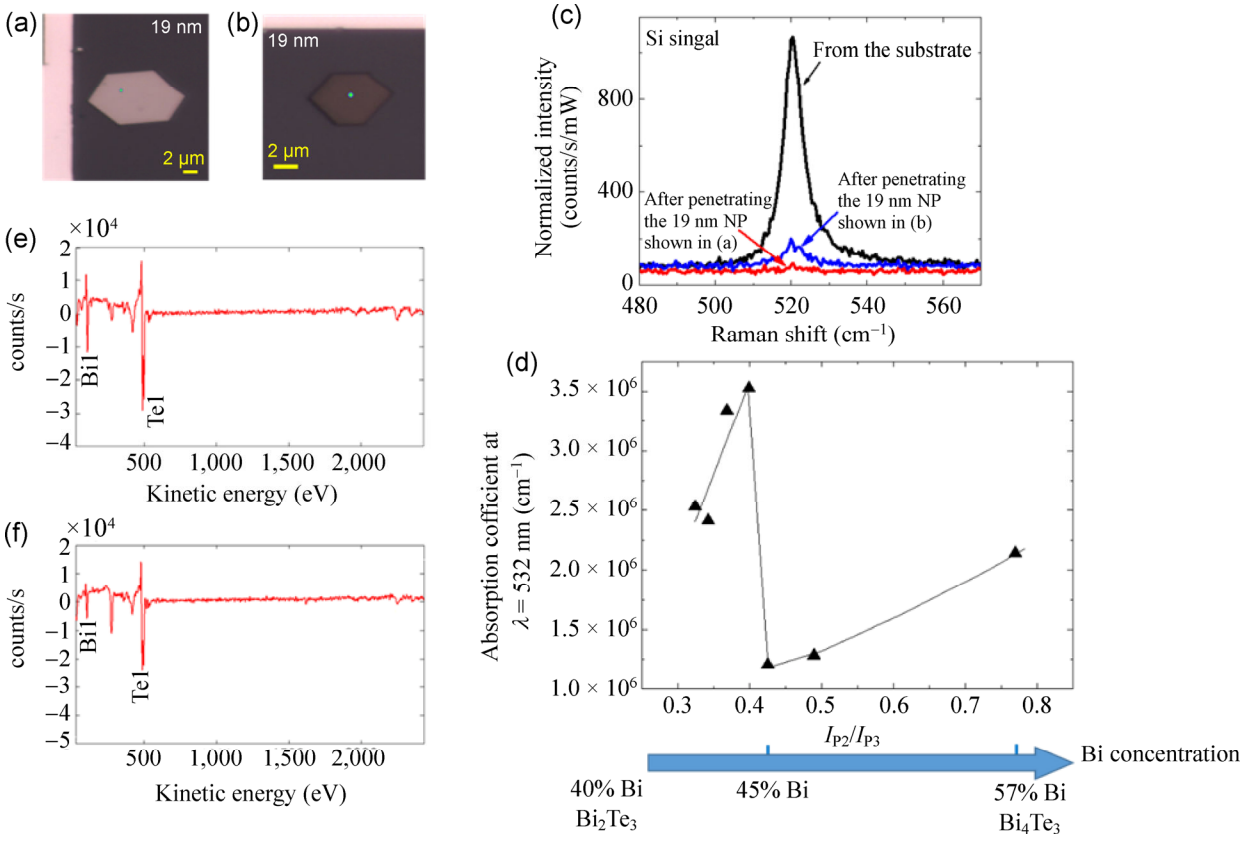

Figure 4 (a) and (b) Optical images of two Bi–Te NPs with the same thickness. Both NPs are on SiO_2 substrates. The green dots show the points at where the laser is focused. (c) Si Raman lines from the substrate and after the laser penetrates the two NPs shown in panels (a) and (b). All spectra were taken with 0.01 mW laser power. (d) Optical absorption coefficient α (at λ = 532 nm) as a function of I_{P2}/I_{P3} which is linked to the concentration of Bi. The solid line is a guide to the eye. (e) and (f) AES spectra of the NPs shown in panels (a) and (b), respectively.

from the Beer's law $I = I_0\exp(-\alpha d)$, where d is the NP thickness, I_0 is the intensity of the Si peak from the substrate, I is the intensity of the Si line after the laser goes through the NPs. The absorption coefficient α is estimated to be 2.14×10^6 and 1.21×10^6 cm^{-1} for the NPs shown in Figs. 4(a) and 4(b), respectively. The higher absorption coefficient of the NP shown in Fig. 4(a) is consistent with its brighter color seen in the optical image.

Figure 4(d) displays α as a function of I_{P2}/I_{P3}. The atomic concentration of Bi in all these probed thin NPs is between 40% (corresponds to Bi_2Te_3) and 57% (corresponds to Bi_4Te_3) as estimated based on the relative intensity I_{P2}/I_{P3} [10]. This estimation of stoichiometry based on Raman spectra is confirmed by the AES measurement. We performed AES studies on the two NPs displayed in Figs. 4(a) and 4(b), and their AES spectra are shown in Figs. 4(e) and 4(f), respectively. The spectra show that the Bi atomic concentration is 57.5% for the NP shown in Fig. 4(a) and is 45.4% for the NP shown in Fig. 4(b). We mark these two concentrations on the horizontal arrow below Fig. 4(d). Therefore, the difference in α for the two NPs with the same thickness (both are 19 nm) could be due to their different stoichiometry.

It is seen in Fig. 4(d) that the optical absorption coefficient α increases when I_{P2}/I_{P3} is between 0.3 and 0.4. It experiences a sharp decline when I_{P2}/I_{P3} is between 0.4 and 0.42 which corresponds to a Bi concentration around 45%. Then α increases again when I_{P2}/I_{P3} is higher than 0.42 (Bi concentration increases to 57%). These results indicate that α is a strong function of the Bi–Te ratio. We conjecture that the sharp change of α occurs when the crystalline structure is close to a stable phase which has 50% Bi atomic ratio (BiTe crystalline structure) [8, 10]. Further investigation is needed to better understand the relation between the optical absorption coefficient in a broad wavelength range and the stoichiometry of the Bi–Te thin NPs.

4 Conclusions

In this paper we have demonstrated that stoichiometric Bi_2Te_3 NPs are oxidized when exposed to intermediate laser power in air. Holes are burned on the sample surfaces when laser power is further increased. The depth of the burned holes increases with the incident laser power. Stoichiometry is found to drastically influence the optical properties and vibrational modes in Bi–Te NPs thinner than 20 nm. As the atomic concentration of Bi varies between 40% and 57% in these thin NPs, Raman modes show characteristic changes as a function of the Bi:Te ratio. Four Raman modes appear in the frequency range 55–140 cm^{-1}. I_{P2}/I_{P3}, ω_{P2}, and ω_{P4} all change monotonically with the atomic concentration of Bi. Optical absorption coefficient α varies significantly with the change of Bi concentration in thin Bi–Te NPs. These results show that controlling the stoichiometry in the Bi–Te NP growth is important for their thermoelectric, electronic, and optical device applications. Further studies are needed to understand the mechanism of oxidation and optical absorption in Bi–Te NPs with different stoichiometry.

Acknowledgements

Acknowledgment is made to the Donors of the American Chemical Society Petroleum Research Fund (No. 53401-UNI10) for support of this research. S. S. thanks Wayne Jennings for his assistance with the AES measurements. R. H. acknowledges support from UNI Faculty Summer Fellowship. T. E. K. acknowledges support by NSF RUI Grant (No. DMR-1206530) and a UNI capacity building grant. R. H. and T. E. K. both acknowledge the support by NSF RUI Grant (No. DMR-1410496). X. P. A. G. acknowledges the NSF CAREER Award program (No. DMR-1151534) for support of research at CWRU.

Electronic Supplementary Material: Supplementary material (further details of the correlation between oxidization and time of laser irradiation) is available in the online version of this article at http://dx.doi.org/10.1007/s12274-014-0567-z.

References

[1] Chen, Y. L.; Analytis, J. G.; Chu, J. H.; Liu, Z. K.; Mo, S. K.; Qi, X. L.; Zhang, H. J.; Lu, D. H.; Dai, X.; Fang, Z. et al. Experimental realization of a three-dimensional topological

insulator, Bi_2Te_3. *Science* **2009**, *325*, 178–181.

[2] Zhang, H. J.; Liu, C. X.; Qi, X. L.; Dai, X.; Fang, Z.; Zhang, S. C. Topological insulators in Bi_2Se_3, Bi_2Te_3 and Sb_2Te_3 with a single Dirac cone on the surface. *Nat. Phys.* **2009**, *5*, 438–442.

[3] Hsieh, D.; Xia, Y.; Qian, D.; Wray, L.; Dil, J. H.; Meier, F.; Osterwalder, J.; Patthey, L.; Checkelsky, J. G.; Ong, N. P. et al. A tunable topological insulator in the spin helical dirac transport regime. *Nature* **2009**, *460*, 1101–1105.

[4] Hasan, M. Z.; Kane, C. L. Colloquium: Topological insulators. *Rev. Mod. Phys.* **2010**, *82*, 3045–3067.

[5] Lee, J.; Kim, J.; Moon, W.; Berger, A.; Lee, J. Enhanced Seebeck coefficients of thermoelectric Bi_2Te_3 nanowires as a result of an optimized annealing process. *J. Phys. Chem. C* **2012**, *116*, 19512–19516.

[6] Yu, F. R.; Zhang, J. J.; Yu, D. L.; He, J. L.; Liu, Z. Y.; Xu, B.; Tian, Y. J. Enhanced thermoelectric figure of merit in nanocrystalline Bi_2Te_3 bulk. *J. Appl. Phys.* **2009**, *105*, 094303.

[7] Wright, D. A. Thermoelectric properties of bismuth telluride and its alloys. *Nature* **1958**, *181*, 834.

[8] Yamana, K.; Kihara, K.; Matsumoto, T. Bismuth tellurides: BiTe and Bi_4Te_3. *Acta Cryst.* **1979**, *B35*, 147–149.

[9] Kim, Y.; Cho, S.; DiVenere, A.; Wong, G. K. L.; Ketterson, J. B. Composition-dependent layered structure and transport properties in BiTe thin films. *Phys. Rev. B* **2001**, *63*, 155306.

[10] Russo, V.; Bailini, A.; Zamboni, M.; Passoni, M.; Conti, C.; Casari, C. S.; Bassi, A. L.; Bottani, C. E. Raman spectroscopy of Bi–Te thin films. *J. Raman Spectrosc.* **2008**, *39*, 205–210.

[11] Teweldebrhan, D.; Goyal, V.; Balandin, A. A. Exfoliation and characterization of bismuth telluride atomic quintuples and quasi-two-dimensional crystals. *Nano Lett.* **2010**, *10*, 1209–1218.

[12] Jones, P.; Huber, T. E.; Melngailis, J.; Barry, J.; Ervin, M. H.; Zheleva, T. S.; Nikolaeva, A.; Konopko, L.; Graf, M. Electrical contact resistance of bismuth telluride nanowires. In *Proceedings of the 25th International Conference on Thermolelectrics,* Vienna, Austria, 2006, pp 693–696.

[13] Qu, D. X.; Hor, Y. S.; Xiong, J.; Cava, R. J.; Ong, N. P. Quantum oscillations and hall anomaly of surface states in the topological insulator Bi_2Te_3. *Science* **2010**, *329*, 821–824.

[14] Ren, Z.; Taskin, A. A.; Sasaki, S.; Segawa, K.; Ando, Y. Optimizing $Bi_{2-x}Sb_xTe_{3-y}Se_y$ solid solutions to approach the intrinsic topological insulator regime. *Phys. Rev. B* **2011**, *84*, 165311.

[15] Kong, D. S.; Chen, Y. L.; Cha, J. J.; Zhang, Q. F.; Analytis, J. G.; Lai, K. J.; Liu, Z. K.; Hong, S. S.; Koski, K. J.; Mo, S. K. et al. Ambipolar field effect in the ternary topological insulator $(Bi_xSb_{1-x})_2Te_3$ by composition tuning. *Nat. Nanotechnol.* **2011**, *6*, 705–709.

[16] Wang, Z. H.; Qiu, R. L. J.; Lee, C. H.; Zhang, Z. D.; Gao, X. P. A. Ambipolar surface conduction in ternary topological insulator $Bi_2(Te_{1-x}Se_x)_3$ nanoribbons. *ACS Nano* **2013**, *7*, 2126–2131.

[17] Tang, H.; Liang, D.; Qiu, R. L. J.; Gao, X. P. A. Two-dimensional transport-induced linear magneto-resistance in topological insulator Bi_2Se_3 nanoribbons. *ACS Nano* **2011**, *5*, 7510–7516.

[18] Kong, D. S.; Dang, W. H.; Cha, J. J.; Li, H.; Meister, S.; Peng, H. L.; Liu, Z. F.; Cui, Y. Few-layer nanoplates of Bi_2Se_3 and Bi_2Te_3 with highly tunable chemical potential. *Nano Lett.* **2010**, *10*, 2245–2250.

[19] Kullmann, W.; Geurts, J.; Richter, W.; Lehner, N.; Rauh, H.; Steigenberger, U.; Eichhorn, G.; Geick, R. Effect of hydrostatic and uniaxial pressure on structural properties and raman active lattice vibrations in Bi_2Te_3. *Phys. Status Solidi B* **1984**, *125*, 131–138.

[20] He, R.; Wang, Z. H.; Qiu, R. L. J.; Delaney, C.; Beck, B.; Kidd, T. E.; Chancey, C. C.; Gao, X. P. A. Observation of infrared-active modes in Raman scattering from topological insulator nanoplates. *Nanotechnology* **2012**, *23*, 455703.

[21] Salazar-Pérez, A. J.; Camacho-López, M. A.; Morales-Luckie, R. A.; Sánchez-Mendieta, V.; Ureña-Núñez, F.; Arenas-Alatorre, J. Structural evolution of Bi_2O_3 prepared by thermal oxidation of bismuth nano-particles. *Superficies y Vacío* **2005**, *18*, 4–8.

[22] Guo, J. H.; Qiu, F.; Zhang, Y.; Deng, H. Y.; Hu, G. J.; Li, X. N.; Yu, G. L.; Dai, N. Surface oxidation properties in a topological insulator Bi_2Te_3 film. *Chin. Phys. Lett.* **2013**, *30*, 106801.

[23] Pine, A. S.; Dresselhaus, G. Raman scattering in paratellurite, TeO_2. *Phys. Rev. B* **1972**, *5*, 4087–4093.

[24] Zhang, J.; Peng, Z. P.; Soni, A.; Zhao, Y. Y.; Xiong, Y.; Peng, B.; Wang, J. B.; Dresselhaus, M. S.; Xiong, Q. H. Raman spectroscopy of few-quintuple layer topological insulator Bi_2Se_3 nanoplatelets. *Nano Lett.* **2011**, *11*, 2407–2414.

[25] Shahil, K. M. F.; Hossain, M. Z.; Teweldebrhan, D.; Balandin, A. A. Crystal symmetry breaking in few-quintuple Bi_2Te_3 films: Applications in nanometrology of topological insulators. *Appl. Phys. Lett.* **2010**, *96*, 153103.